Forschung im Ingenieurwesen (2025)89:62
https://doi.org/10.1007/s10010-025-00828-9

ORIGINALARBEITEN/ORIGINALS

Parametric study and inverse design of perforated silicone auxetic structures

Tamás Vargovics[1] · Attila Kossa[1]

Received: 2 October 2024 / Accepted: 28 February 2025

Abstract

A parametric analysis was conducted to determine the influence of geometric parameters on the Poisson's ratio of an auxetic structure. The results show that, for the selected geometry, the Poisson's ratio can be precisely adjusted between -0.8 and 0.2 by modifying the geometry. Four different auxetic structures were analyzed through both experimental measurements and finite element simulations, demonstrating a strong correlation between numerical and test results until the onset of wrinkling, which introduces deviations in transverse deformations. The wrinkling phenomenon was identified in all examined auxetic structures. The critical stretch values at which wrinkling occurs were quantified using single-view motion tracking without the need for side-view imaging. A sixth-order Ogden hyperelastic model was fitted to uniaxial test data and refined using a custom parameter-fitting algorithm, ensuring accurate material representation. The developed finite element model was extended to three-dimensional cases, and the auxetic behavior of a 3D auxetic cube was analyzed, highlighting its anisotropic properties. The proposed methodology enables the targeted design of auxetic structures with predefined mechanical responses, making it applicable to a wide range of engineering applications.

Parametrische Studie und inverses Design von gelochten Silikon-Auxetic-Strukturen

Zusammenfassung

Eine parametrische Analyse wurde durchgeführt, um den Einfluss geometrischer Parameter auf die Poissonzahl einer auxetischen Struktur zu bestimmen. Die Ergebnisse zeigen, dass für die gewählte Geometrie die Poissonzahl präzise zwischen -0,8 und 0,2 durch Anpassung der Geometrie eingestellt werden kann. Vier verschiedene auxetische Strukturen wurden sowohl experimentell als auch mittels Finite-Elemente-Simulationen untersucht, wobei eine starke Übereinstimmung zwischen den numerischen und experimentellen Ergebnissen bis zum Auftreten von Wrinkling festgestellt wurde. Das Wrinkling-Phänomen führte zu Abweichungen in den Querdeformationen. Wrinkling wurde in allen untersuchten auxetischen Strukturen identifiziert, und die kritischen Dehnungswerte, bei denen es auftritt, wurden mittels Einzelansicht-Motion-Tracking quantifiziert, ohne dass Seitenansichten erforderlich waren. Ein hyperelastisches Ogden-Modell sechster Ordnung wurde an uniaxiale Zugversuche angepasst und mit einem eigenen Parameteranpassungsalgorithmus weiter optimiert, um eine präzise Materialdarstellung zu gewährleisten. Das entwickelte Finite-Elemente-Modell wurde auf dreidimensionale Fälle erweitert, wobei das auxetische Verhalten eines 3D-auxetischen Würfels analysiert und seine anisotropen Eigenschaften hervorgehoben wurden. Die vorgeschlagene Methodik ermöglicht die gezielte Konstruktion von auxetischen Strukturen mit vordefinierten mechanischen Eigenschaften und ist somit für ein breites Spektrum ingenieurtechnischer Anwendungen einsetzbar.

1 Introduction

The advancement of new technologies demands novel materials with increasingly specific properties. Auxetic structures, a type of mechanical metamaterial, have gained attention due to their unique negative Poisson's ratio [1], which differentiates them from conventional materials. While nat-

These authors contributed equally to this work.

✉ Attila Kossa
kossa@mm.bme.hu

[1] Faculty of Mechanical Engineering, Department of Applied Mechanics, Budapest University of Technology and Economics, Műegyetem rkp. 3., 1111 Budapest, Hungary

Published online: 04 April 2025

urally occurring, auxetic materials have only recently been extensively studied. For isotropic materials, Poisson's ratio typically ranges from 0 to 0.5 in the small-strain regime, whereas in auxetic materials, it is strain-dependent due to significant deformations [2]. Cellular materials consist of repetitive unit cells, forming a structured microarchitecture that influences their macroscopic behavior.

Initially, researchers believed auxetic materials were rare in nature, but recent studies have identified them in ceramics, polymers, and even cat skin [3]. Certain metals with special lattice structures also exhibit auxetic behavior. The focus today is on artificial auxetic structures, particularly in biomedical applications. Auxetic stents offer advantages over conventional designs, such as maintaining or even increasing their length after insertion. Abbaslou et al. [4] conducted finite element simulations and confirmed the mechanical suitability of auxetic stents, a conclusion also supported by Vellaparambil et al. [5] and Behinfar et al. [6], demonstrating their feasibility.

Other medical applications include implants, such as auxetic spinal disc replacements for lumbar hernia [7]. Traditional implants can deform under long-term pressure, whereas auxetic implants offer improved durability. Jiang et al. found that test specimens withstood practical everyday loads, demonstrating promising structural properties.

Auxetic structures have promising applications in energy absorption and protective equipment across industries such as automotive, aerospace, military, and sports [8–10]. Studies show that auxetic shells filled with aluminum foam absorb more energy than separate components, enhancing impact resistance [11, 12]. 3D lattice structures have also been explored for energy absorption [13]. Faraci et al. [14] designed an auxetic face mask that distributes impact energy more evenly than conventional designs, while Tomita et al. [15] developed a seat-mounted head protection system, demonstrating superior absorption capacity.

Auxetic materials also enable inverse design approaches, where geometry is optimized for a specific Poisson's ratio using machine learning [16]. Ebert et al. introduced an ABC weave-based method for generating structures implicitly, without predefined unit cells [17].

One of the most promising fields for auxetic materials is soft robotics. Grossi et al. developed a caterpillar-inspired robot with an auxetic frame, achieving natural motion dynamics [18]. Auxetic structures are also key for bending actuators, essential in prosthetics, artificial muscles, and robotic components [19]. Lee et al. introduced a 3D printable auxetic tubular spring for hopping robots, offering improved gait stability and energy storage compared to traditional linear springs [20].

Analytical approaches in the literature describe auxetic metamaterials using mathematical models [21, 22]. Rafsanjani and Pasini developed bistable auxetic structures inspired by ancient geometric motifs, conducting uniaxial tensile tests to analyze Poisson's ratio and force-displacement behavior [23]. These structures exhibit nonlinear deformation, making them suitable for switches and actuators. Other innovations include auxetic superhydrophobic surfaces [24] and SMA-based auxetic elements, which could be applied in robotics [25].

In the context of cellular structures, experimental results are often compared with numerical findings obtained through finite element methods, as demonstrated by Dara et al. [26, 27], who investigated nature-inspired lattice structures, including an open lattice design based on the Victoria water lily, highlighting their enhanced stiffness and specific energy absorption capabilities. A structured approach to optimizing geometric configurations for enhanced mechanical performance has been explored in various studies, such as [28], where a nature-inspired 2.5D infill structure was developed and systematically compared to existing designs to improve energy absorption efficiency.

The objective of this study is to establish a systematic methodology for designing planar auxetic structures with tailored Poisson's ratio at predefined stretch values. To achieve this, we develop and validate finite element models, supported by experimental measurements, to accurately capture the mechanical behavior of auxetic materials. A parametric analysis is introduced to explore the influence of geometric parameters on auxetic behavior, providing a framework for controlled structure design. The impact of wrinkling on deformation characteristics is also investigated to enhance the understanding of its role in practical applications. The proposed methodology is intended to serve as a generalizable approach for modeling and designing auxetic structures beyond the specific cases analyzed in this work.

The paper is organized as follows. Section 2.1 presents the examined auxetic structures and describes the manufacturing process used to fabricate them. Section 2.2 details the experimental setup, including the methodology for calculating Poisson's ratio. Section 2.3 provides a description of the finite element model employed in this study. In Section 3.1, we introduce the fitted hyperelastic material model, while Section 3.2 compares the experimental and numerical results. Section 4 presents the parametric analysis performed on the selected auxetic geometry, highlighting the influence of geometric parameters on auxetic behavior. Finally, after the discussion and conclusion sections, the appendix includes an additional case study of a 3D auxetic structure currently under development.

2 Materials and methods

2.1 Material description and specimen preparation

This study examines four auxetic structures, each with a unique geometry. The test specimens have a cellular structure, comprising unit cells. They have a 2D geometry and are constructed from silicone sheets with perforations. The auxetic behavior is a consequence of the shape and positioning of these perforations. The elementary cells are uniform and follow one another in a defined order, thereby belonging to ordered cellular structures. Each specimen is encased in a rectangular enclosure measuring 120×90×1 mm. The upper and lower portions of the specimens are constructed with a 15 mm margin. The structures themselves are arranged in a 90×90 mm block with a distinct unit cell number. The CAD model of the test specimens are shown in Fig. 1. Subsequently, we employed the STR notation, accompanied by the number of the structure, in order to streamline the document. The layout of the unit cells are a collection of geometric elements, dimensions and constraints. However, the main characteristics of each unit cell can be influenced by changing two parameters for each design.

In the majority of analogous studies, TPU (thermoplastic polyurethane) was employed as the material of choice, with 3D-printing as manufacturing technology [8, 10, 29–33]. However, in this instance, a different approach was taken. We employed a laser cutting machine to fabricate the test specimens, which represents an automated material separation process based on thermal energy [34]. In this study, an ALFA LCE-2 (9060) laser cutting and engraving machine [35] was utilized. This is a 900×600 mm working area tool, specially designed to cut non-metallic materials. It is capable of cutting with a power of 80–100 W. The device in question has a carbon dioxide resonator gas, is water-cooled, and its cutting speed that can be adjusted between 0 and 24 000 mm/min. It is controlled by a DPS system and the fumes generated during operation are extracted by a centrifugal fan. The aim was to reduce the effect of temperature as much as possible, while maintaining high quality and accuracy of the resulting cutting edges. Following several iterations, the optimal cutting speed was determined to be 20 mm/s, and the maximum power to be used was set to be 50% of the maximum power of the equipment. Another advantage of the technology is that it requires minimal post-production work. In conclusion, this material separation technology has enabled the production of sufficiently accurate, high quality specimens in a relatively short and straightforward process.

2.2 Experimental setup

Uniaxial tensile tests were conducted on specimens designed and fabricated in accordance with the specifications outlined previously. $L_0 = 90$ mm represents the original length of the specimens, $\Delta L = 100$ mm denotes the applied maximum displacement, and 100 ms is the sampling time. In order to achieve a quasi-static measurement, the velocity of the upper, moving fixture has been set to $v = 5.58\,\mathrm{mm/min}$, resulting a low strain rate $\dot{\varepsilon} = 0.001$. The force values were recorded using the built-in force measuring cell of the material test equipment (Instron 3345 Universal Mechanical Material Tester).

To determine the transverse deformation of the investigated auxetic structures, we recorded high-resolution video footage, as this method is commonly used by many researchers studying auxetic structures [8, 29, 31]. The measurements were recorded on video using a Fujifilm X-H2 digital camera, equipped with a Fujinon Lens (XF16-80mmF4 R OIS). The actual video resolution of the camera is 7680×4320 pixels (8K resolution). The evaluation was carried out using the so-called Motion Tracker Beta, a freely available, open-source motion-tracking program

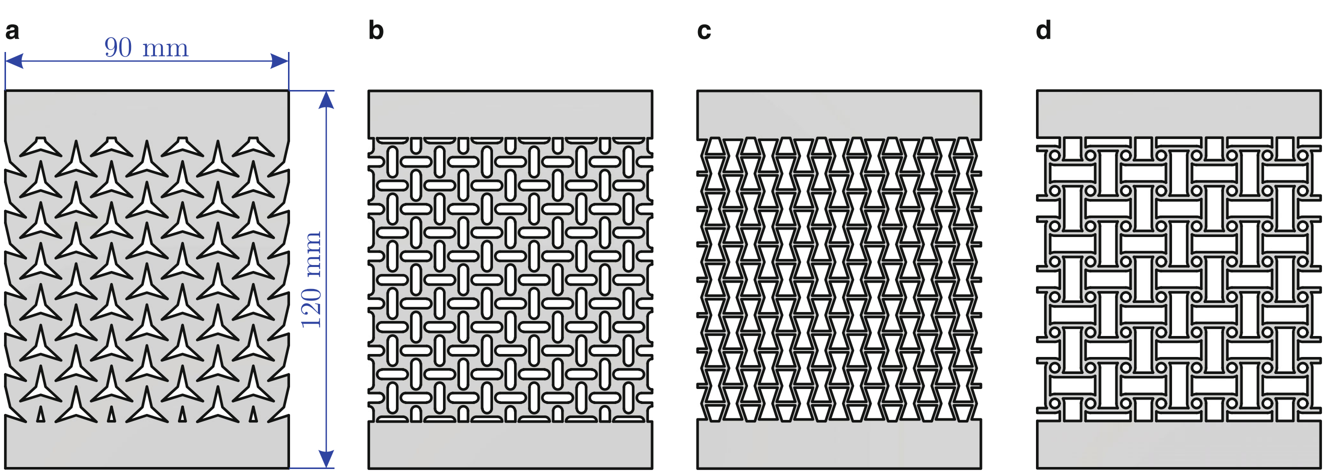

Fig. 1 CAD models of the specimens: **a** STR1, **b** STR2, **c** STR3, **d** STR4

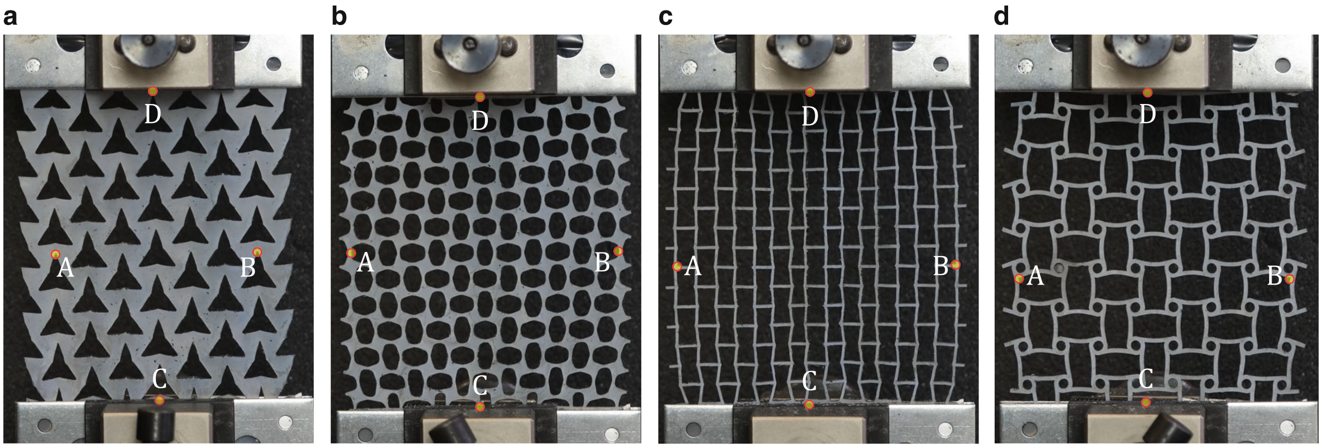

Fig. 2 Images of the four investigated auxetic structures at a stretch value of λ = 1.16, showing their deformed configurations. The A, B, C, and D points are marked in each image and were tracked using motion tracking software to analyze transverse deformation and determine the Poisson's functions

[36]. The evaluation process involved the following steps: reading and opening the files, defining the points to be tracked, tracking, evaluation and exporting the results.

For auxetic structures, there is no standardized method for determining the Poisson's ratio, as its value strongly depends on which regions and points of the material are selected for motion tracking. This has been thoroughly discussed in the work of Yolcu and Baba [37]. Consequently, when using experimental results to validate finite element models, we have the flexibility to choose arbitrary points for Poisson's ratio calculations. Notably, tracking multiple points and averaging the results is also a possible approach [37].

For the four investigated geometries, Fig. 2 illustrates the points whose displacements were used to compute the strain-dependent Poisson's ratio. The A and B points were used to determine the transverse stretch, while the C and D points were used to calculate the axial stretch. Let L_0 denote the initial distance between C and D, and H_0 the initial distance between A and B. The instantaneous distances are denoted by L and H, respectively. The axial and transverse stretch values can then be calculated as follows:

$$\lambda = \frac{L}{L_0}, \qquad \lambda_T = \frac{H}{H_0}. \tag{1}$$

Using these stretch values, we introduce the Poisson function for large deformations, as proposed by Beatty [38]:

$$\nu = -\frac{\ln\lambda_T}{\ln\lambda}. \tag{2}$$

To ensure accuracy and eliminate potential errors, each measurement was performed on five different specimens for each geometry. It is worth noting that in most studies on auxetic structures, Poisson's ratio is typically determined using the above formula. However, in some cases, researchers also introduce the concept of the incremental Poisson's ratio, which establishes a relationship between infinitesimal strain increments [39–44].

2.3 Finite element modelling

In this study, finite element analyses were conducted using Simulia Abaqus version 2022 software. Standard, static, two-dimensional simulations were performed on simplified, deformable geometries, as illustrated in Fig. 3, on structure STR4. The points to be tracked were added in a manner analogous to that described previously. A homogeneous, isotropic, incompressible material was implemented, with its behavior described by the sixth-order Ogden hyperelastic model. It should be noted that thermal, dynamic and failure effects and models have not been included in this analysis. It is imperative to activate the *NLGEOM* option because the analysis will result in large deformations and strains. An *ENCASTRE* boundary condition was applied to the lower edge, which entails a complete gripping action with all degrees of freedom constrained. For the left-hand edges of the geometry, a symmetry in the horizontal direction was specified. A vertical displacement of 100 mm was defined for the top edge, with the horizontal displacement held at zero. The defined boundary conditions are illustrated in Fig. 3. The structures were meshed using general plane-stress linear continuum elements, as demonstrated in the corresponding column of Table 1.

Before selecting the final mesh resolution for the finite element simulations, we conducted a detailed mesh dependency analysis to ensure that the results were not significantly influenced by the mesh size. We tested 11 different meshing strategies, systematically refining the mesh

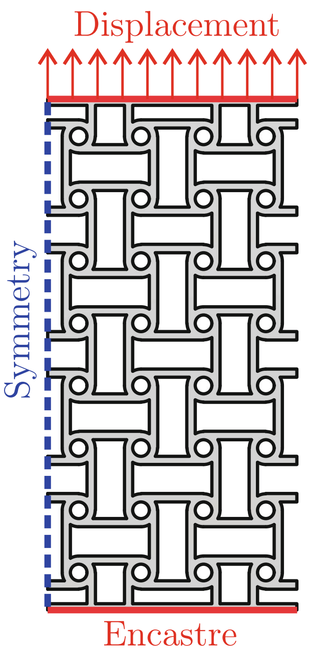

Fig. 3 Boundary conditions and loading during the FE simulations

and analyzing the resulting variations in reaction force and transverse deformations. The finest mesh contained approximately 10 times more elements than the mesh ultimately used in the manuscript. The comparison showed that the difference in the computed reaction force and reference point displacement between the finest mesh and the selected one was less than 1%, indicating converged results. Based on these findings, the selected mesh configuration provided a good balance between computational efficiency and numerical accuracy. This validated mesh ensures that the simulations remain both quantitatively and qualitatively reliable without excessive computational cost.

It is crucial to model accurately the mechanical behavior of the silicone base material in order to gain a deeper understanding of its characteristics. When analysing hyperelastic materials, it is advisable to utilize data from three distinct homogeneous deformation types: uniaxial loading, biaxial loading, and planar loading. Within the scope of this research, it was possible to perform uniaxial experiments, which were conducted using a uniaxial Instron 3345 Universal Mechanical Material Tester. The material is subjected to significant axial displacements, resulting in elongations of more than four times the original dimensions. The objective is to conduct quasi-static measurements, which are crucial for the elimination of viscoelastic effects. These effects were considered indirectly in our study, with the use of essentially slow experiment data being considered authoritative. Failure effects were not taken into account, with the data being fitted up to the moment before failure.

The results of the uniaxial tensile tests were employed as a foundation for the construction of the material model. However, in order to more accurately reflect the material properties, a virtual equibiaxial data set was also generated. This was attained by multiplying the uniaxial data by a constant (1.5), which, despite the fact that the relationship is a function of some kind (not a constant), is a good approximation based on measurement data available in the literature [45, 46].

To accurately describe the mechanical behavior of the base material, we systematically tested all available hyperelastic models in Abaqus by fitting them to our experimental data using the software's built-in parameter-fitting module. Among the tested models, the sixth-order Ogden model provided the lowest fitting error, indicating the highest accuracy in capturing the material's nonlinear stress-strain behavior. Following the selection of the sixth-order Ogden model, we further refined its parameters using a custom parameter-fitting algorithm implemented in Wolfram Mathematica. This additional step allowed us to optimize the material parameters beyond the default Abaqus fitting, ensuring a more precise representation of the experimental data. Based on these findings, we concluded that the sixth-order Ogden model offers the most reliable approximation for the investigated material within the studied strain range.

It is worth noting that some studies completely disregard the behavior of the hyperelastic model under biaxial conditions and fit hyperelastic models solely based on uniaxial measurement data. However, it is important to emphasize that the tested specimens experience a multiaxial stress state. Therefore, it is advisable to use a hyperelastic model that provides accurate and reliable results even under complex stress conditions. The strain energy function of the sixth-order, incompressible, Ogden hyperelastic model is expressed as

$$W = \sum_{k=1}^{6} \frac{2\mu_k}{\alpha_k^2} (\lambda_1^{\alpha_k} + \lambda_2^{\alpha_k} + \lambda_3^{\alpha_k} - 3)\,. \tag{3}$$

Table 1 Main properties of the meshes of the structures

Structure	Global Seed size	Element type	Element number	Node number
STR1	0.3 mm	CPS4/CPS3	45 280 (44 662/618)	47 137
STR2	0.3 mm	CPS4/CPS3	29 280 (28 488/792)	31 894
STR3	0.3 mm	CPS4	19 480	23 239
STR4	0.3 mm	CPS4/CPS3	18 478 (18 134/344)	21 254

The material parameters to be determined are μ_k and α_k with $k = 1 \ldots 6$. Furthermore, the principal stretches are represented by λ_1, λ_2 and λ_3. Closed-form expressions can be derived for the engineering stress solutions in each loading case:

$$
\begin{aligned}
P_U &= \sum_{k=1}^{6} \frac{2\mu_k}{\alpha_k} (\lambda^{\alpha_k - 1} - \lambda^{-\alpha_k/2 - 1}) \,, \\
P_B &= \sum_{k=1}^{6} \frac{2\mu_k}{\alpha_k} (\lambda^{\alpha_k - 1} - \lambda^{-2\alpha_k - 1}) \,, \\
P_P &= \sum_{k=1}^{6} \frac{2\mu_k}{\alpha_k} (\lambda^{\alpha_k - 1} - \lambda^{-\alpha_k - 1}) \,.
\end{aligned}
\tag{4}
$$

The engineering stress associated with uniaxial loading is denoted by P_U, while that associated with equibiaxial loading is denoted by P_B. The stress solution corresponding to the planar tension loading is represented by P_P. A quality function based on the RMS (root mean squared) relative error was employed in the fitting of the material parameters:

$$
Q = \sqrt{\frac{1}{n} \sum_{i=1}^{n} \left(\frac{P^{exp} - P^{model}}{P^{exp}} \right)^2} \,, \tag{5}
$$

where i denotes the number of experimental data points. The objective of the fitting process was to identify the global minimum of the error function, i.e. to minimize the discrepancy between the measured and the calculated stress values. This was achieved by iteratively varying the values of the parameters. A variety of algorithms are available for this purpose. In this instance, we employed Wolfram Mathematica's NMinimize built-in function.

3 Results

3.1 Fitted hyperelastic model

For the uniaxial tensile tests, we conducted five independent measurements on geometrically identical specimens to ensure repeatability and reliability. The longitudinal stretch was determined using tracking points placed on the specimen surface, minimizing the influence of potential clamping effects near the grips. The resulting force-stretch curves from the five tests exhibited negligible deviation confirming the consistency of the measurements. The maximum observed variation between tests remained well within the display line thickness, indicating a high level of repeatability. To further enhance the accuracy of our hyperelastic material model fitting, we used the average of these five measurements as the representative dataset. These results validate that the adopted measurement approach provides reliable, reproducible, and precise data for subsequent numerical analyses. In the literature, it is widely accepted that performing measurements on at least five specimens is a standard methodology to filter out potential measurement errors and ensure repeatability, providing statistically robust experimental data [47, 48].

It is essential to highlight that the fitting was conducted up to $\lambda = 3$, as this range is pertinent to the study in question. The resulting minimum value of the quality function is $Q = 5.6\%$, whereas the coefficients of determination for the two data sets are $R_U^2 = 0.9922$ and $R_B^2 = 0.9932$. The curves resulting from the measurements and those constructed with the fitted parameters are presented in Fig. 4. The results demonstrate that the model solutions align well with the measurement points, which provides evidence that a robust constitutive model has been constructed. The fitted model parameters are listed in Table 2.

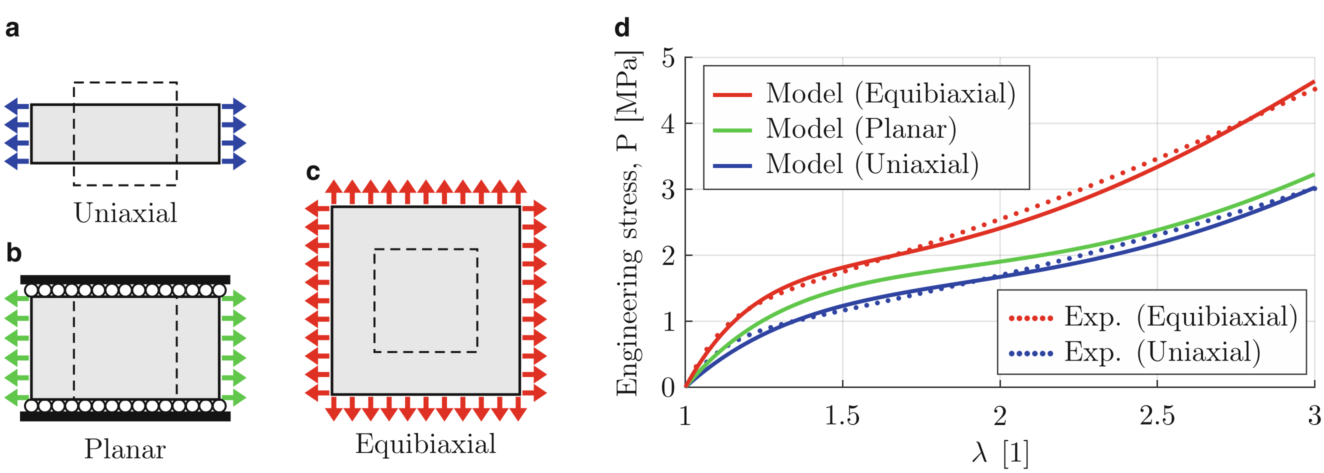

Fig. 4 **a**–**c** Homogeneous loading cases used for hyperelastic parameter fitting: **a** uniaxial loading, **b** planar loading, and **c** equibiaxial loading. **d** Comparison of experimental data and the fitted hyperelastic model, showing the accuracy of the selected sixth-order Ogden model in capturing the material's nonlinear mechanical response

Table 2 The fitted parameters of the sixth-order Ogden hyperelastic model

k	μ_k [MPa]	α_k
1	–464.623	0.8815
2	223.866	0.6547
3	63.973	3.2124
4	–158.813	2.0417
5	–35.995	3.4344
6	373.043	1.3582

3.2 Comparison of experimental and numerical results for auxetic structures

The variation of the transverse stretch values obtained from both experimental measurements and finite element simulations as a function of axial stretch is presented in Fig. 5 for all examined auxetic structures, up to 15% engineering strain. In the figure, the experimentally measured values are represented in blue, while the finite element simulation results are shown in red. Due to the inherent characteristics of the four examined auxetic structures, their mechanical responses differ; however, the numerical results closely match the experimental data up to the onset of wrinkling, confirming the reliability of the simulation model.

During the experiments, five different specimens were tested for each auxetic structure. Since the obtained measurement values showed no significant deviation in either trend or magnitude, a representative dataset was selected for comparison in Fig. 5. The wrinkling phenomenon was observed in all four auxetic structures, and its presence is clearly identifiable from the comparison of the measured and simulated data. Although only a single camera perspective was used for deformation analysis, wrinkling was visibly recognizable in the video recordings. In the experimental data, the onset of wrinkling is more pronounced, as it distinctly marks the stretch value at which the sheet loses stability and wrinkling occurs.

Due to wrinkling, the in-plane projection of the transverse deformations significantly increases. For the investigated auxetic structures, wrinkling occurred at approximately the following stretch values: 1.09, 1.075, 1.065, and 1.05, corresponding to the STR1, STR2, STR3, and STR4 geometries, respectively. It is important to emphasize that the stretch threshold for wrinkling onset strongly depends on the applied boundary conditions.

Our primary objective is to understand and describe the behavior of auxetic structures in the absence of wrinkling. To achieve this, the results presented in Fig. 5 are also displayed over the $\lambda = 1 \ldots 2$ deformation range, as shown in Fig. 6. It can be observed that after the onset of wrin-

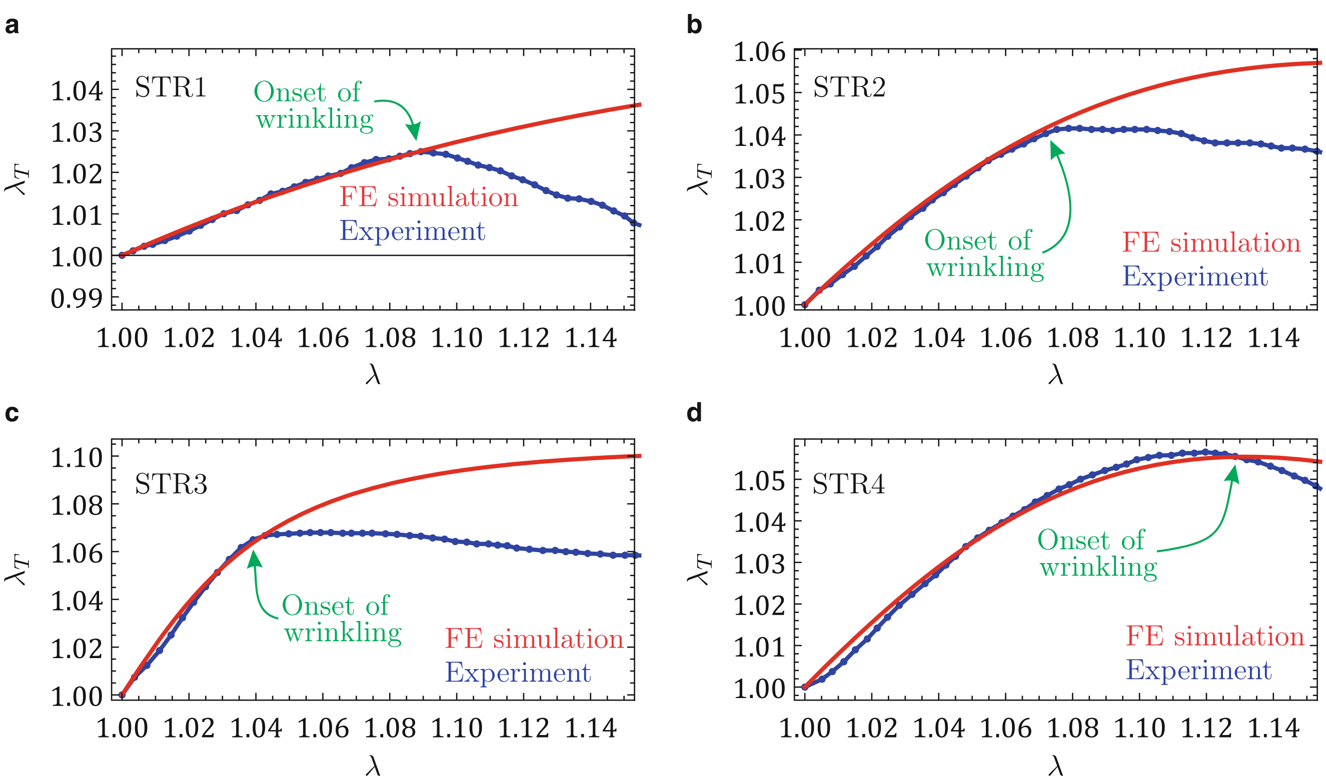

Fig. 5 Comparison of transverse stretch values obtained from experiments (blue data points) and finite element simulations (red curves) for the four investigated auxetic structures: **a** STR1, **b** STR2, **c** STR3, and **d** STR4. The green marker indicates the stretch threshold at which wrinkling was observed in the experimental tests

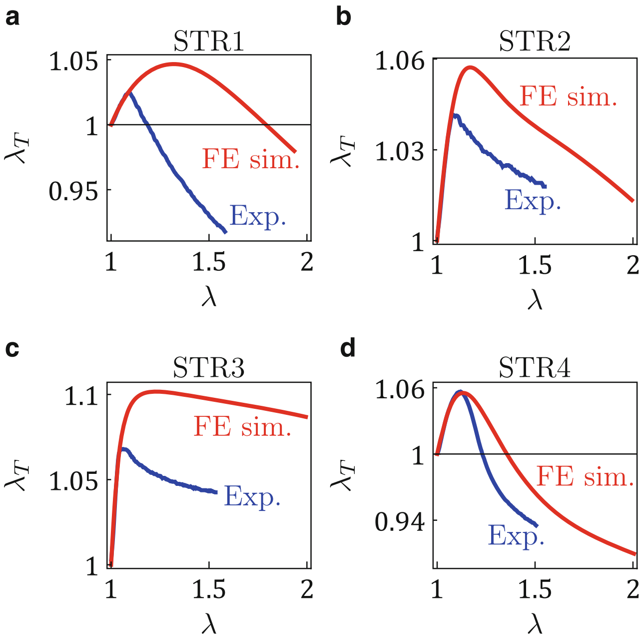

Fig. 6 Comparison of transverse stretch values obtained from experiments (blue data points) and finite element simulations (red curves) for the four investigated auxetic structures: **a** STR1, **b** STR2, **c** STR3, and **d** STR4. Stretch range: $\lambda = 1 \ldots 2$

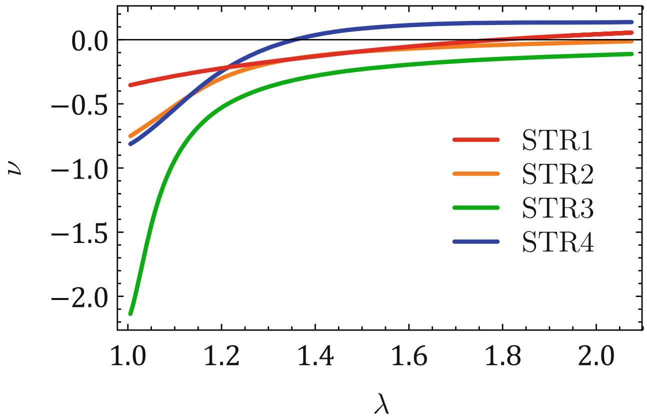

Fig. 7 Variation of the Poisson's ratio as a function of axial stretch λ, determined from finite element simulations for the four investigated auxetic structures. The results for each structure are represented using different colors: STR1 (red), STR2 (orange), STR3 (green), and STR4 (blue)

kling, the trend of the measured data remains similar to the values obtained from finite element simulations. However, due to wrinkling, a significant deviation is observed in the transverse stretch values.

The finite element simulation data allow us to illustrate the variation of the large-strain Poisson's ratio as a function of axial stretch. The Poisson's ratios obtained for the four different auxetic geometries are presented in Fig. 7. From

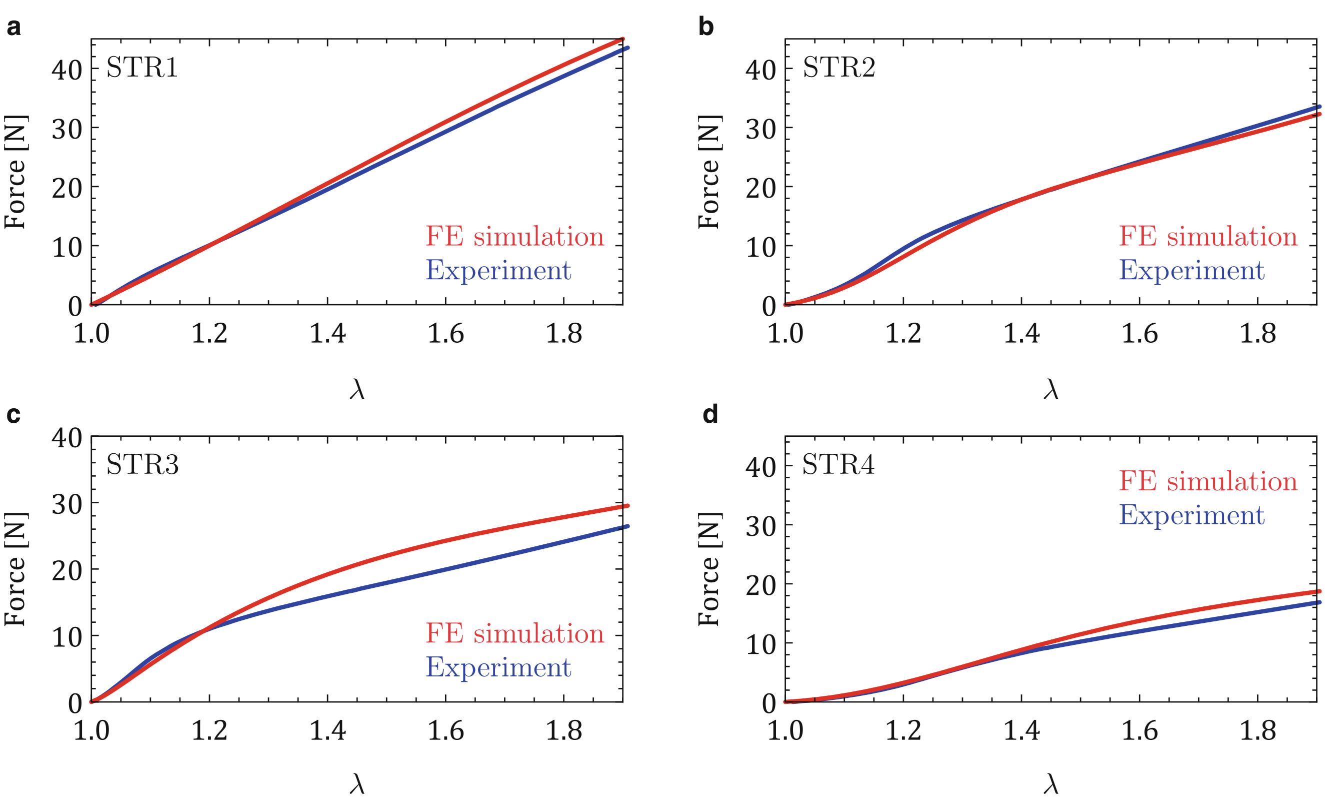

Fig. 8 Comparison of reaction force values obtained from experiments (blue curves) and finite element simulations (red curves) for the four investigated auxetic structures: **a** STR1, **b** STR2, **c** STR3, and **d** STR4

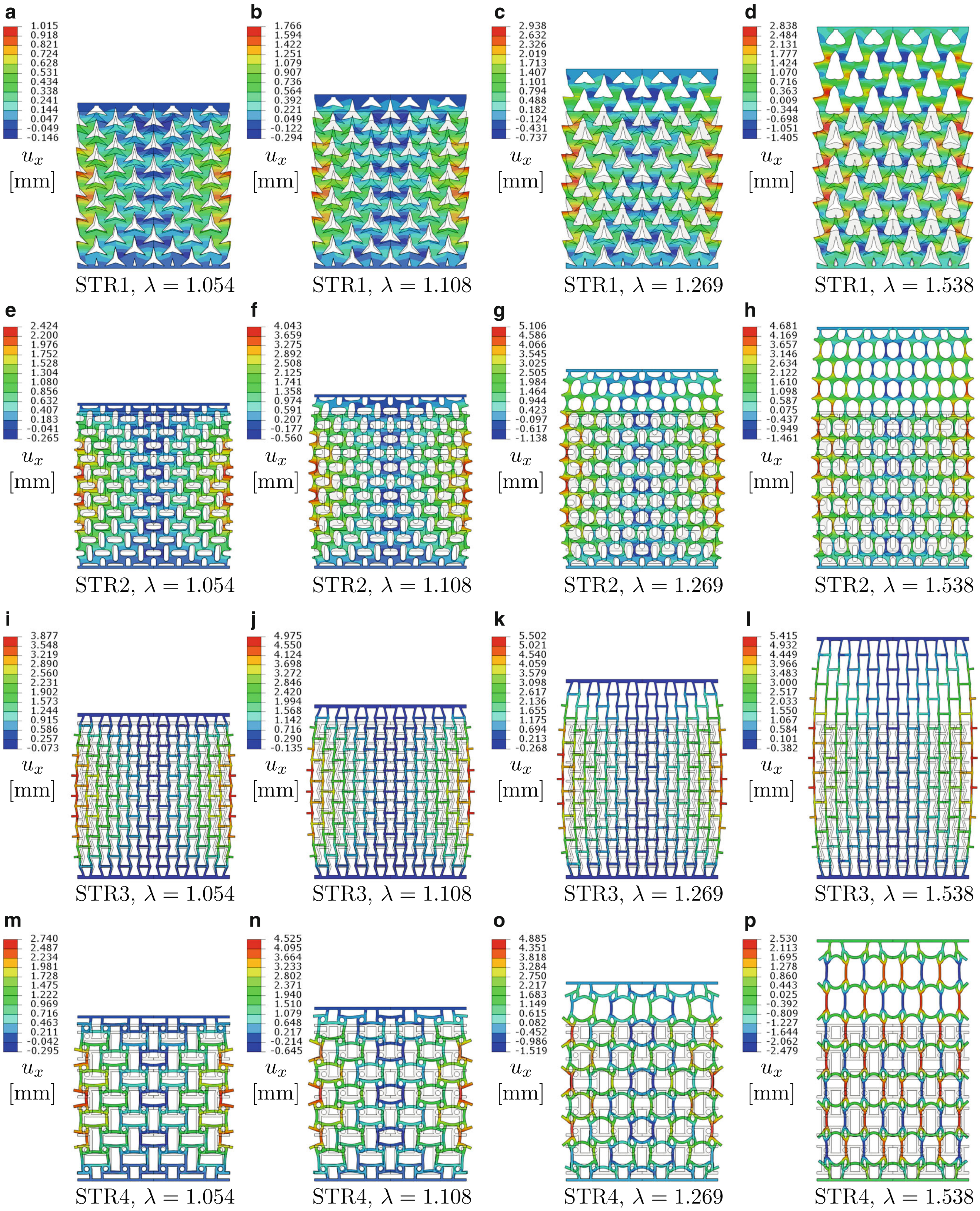

Fig. 9 Deformed shapes of the auxetic structures at four different stretch values, with the initial configurations shown in semi-transparent grayscale for reference. The color scale represents transverse displacements, where positive values indicate expansion. Note that the color scale varies between subfigures based on the deformation range

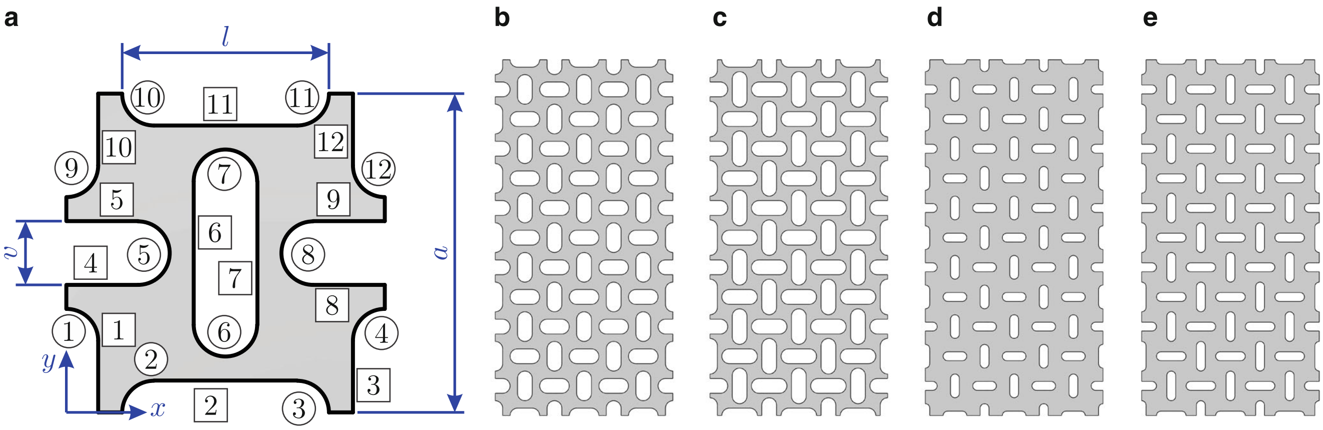

Fig. 10 Unit cell, and sample configurations with $\tilde{v}$ and $\tilde{l}$ values: **a** 1,1, **b** 1,5, **c** 5,1, **d** 5,5. The numbers on a circle basis represent the arcs, while the numbers on a square basis the lines of the geometry

the results, it can be concluded that all four investigated auxetic structures exhibit negative Poisson's ratios, which is consistent with the initial expectations. As the axial stretch increases, the Poisson's ratio values also increase. Within the investigated $\lambda = 1 \ldots 2$ range, only the STR1 and STR4 structures reach and exceed the zero Poisson's ratio threshold. The initial Poisson's ratio values for each structure are as follows: STR1: $\nu = -0.359$, STR2: $\nu = -0.764$, STR3: $\nu = -2.194$, STR4: $\nu = -0.824$.

To validate the finite element model, we compare the reaction forces obtained from experimental measurements and simulations. Fig. 8 presents this comparison using the same plotting range for all cases. The force-stretch relationships exhibit a nonlinear behavior in all cases, which results from both material and geometric nonlinearity. Despite the occurrence of wrinkling in all four structures, its impact on the reaction forces remains minimal. The force values obtained from measurements and simulations show good agreement, with the only notable deviation observed for the STR3 structure.

The deformed shapes of each auxetic structure at four different stretch values are presented in Fig. 9. Each subfigure displays the deformed configuration, while the initial shape is shown in semi-transparent grayscale for reference. The color mapping in each subfigure represents the horizontal displacements, where positive values indicate an increase in transverse dimensions. It should be noted that the scales of the legends differ across the subfigures.

4 Parametric analysis

In the preceding sections, we examined a number of auxetic structures, each of which was represented by a distinct geometric configuration. The subsequent stage of our investigation involves the application of a parametric study, which serves to optimize the geometry of each structure in accordance with a set of specified requirements. Abaqus was employed as a tool for this purpose as well. The parametric study can be conducted by scripting the input code of the Abaqus model in Python environment.

In designing the auxetic structure for this study, it was necessary to select a specific geometric configuration that would best suit our objectives. Among the various auxetic geometries available in the literature, we chose the STR2 design due to its smooth geometry, which minimizes stress concentrations, and its suitability for achieving the desired mechanical response. This selection was also influenced by the need for a practical and manufacturable structure that maintains auxetic behavior across a wide deformation range. The following analyses and parametric studies are based on this selected geometry, allowing us to systematically explore its influence on Poisson's ratio and optimize its design for potential applications.

The following steps were employed to create the analysis: construction of a base model, manipulation of its source code in Python, execution of the parameterised source code in Abaqus, and exportation and evaluation of the results. The base model was constructed using the software's graphical user interface (GUI), but with different dimensions employed for optimal parametrization. The distribution of the unit cells is identical to that of the original specimen (6×6), but their dimensions are different, with a length of $a = 8$ mm per side. Another modification is the amount of displacement, which was fixed at 80 mm instead of 100 mm to prevent excessive elongations. The unit cell can be observed in Fig. 10.

The parametrization was achieved by introducing two parameters, $\tilde{l}$ and $\tilde{v}$, which alter the length and width of the cut-outs in that order. It is of particular significance to note that $\tilde{l}$ increases the length (l) and $\tilde{v}$ decreases the width (v). A loop was created in the code where the aforementioned

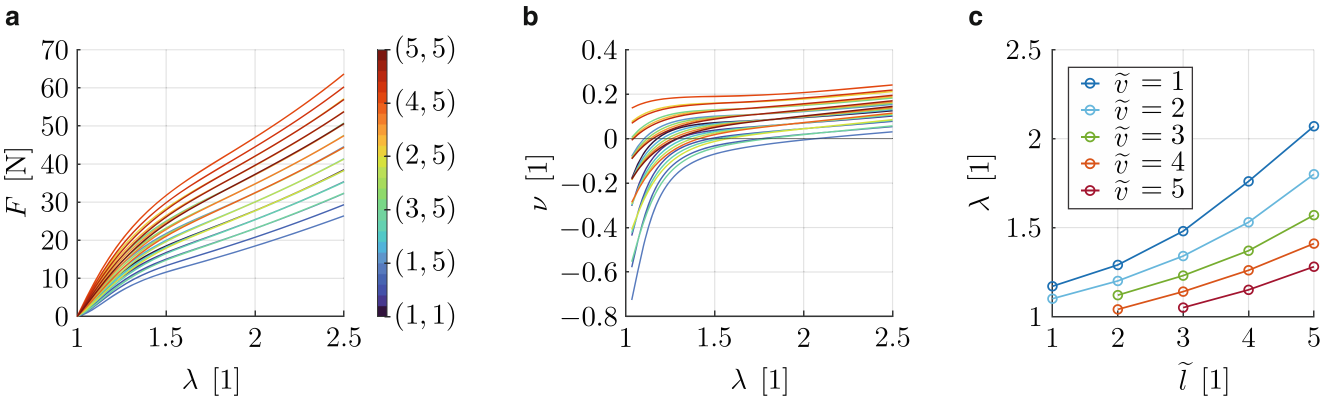

Fig. 11 The resulting characteristics (with $\tilde{v}$ and $\tilde{l}$ values): **a** force-axial stretch functions, **b** Poisson functions; and **c** the value of axial stretch associated with zero Poisson's ratio for each structure displayed in the function of parameters

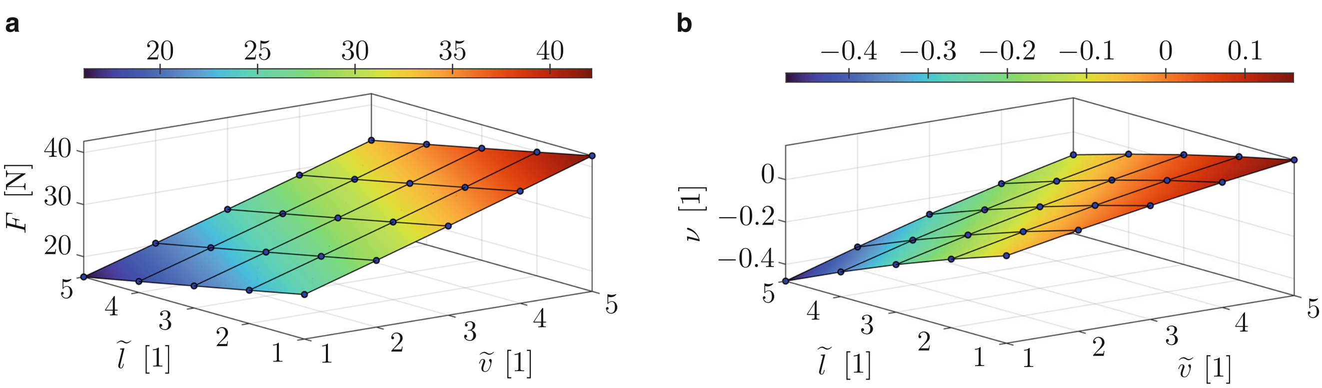

Fig. 12 Influence of geometric parameters on mechanical response. **a** Dependence of the tensile force F on the geometric parameters $\tilde{v}$ and $\tilde{l}$, with results corresponding to $\lambda = 1.85$. **b** Dependence of the Poisson's ratio on $\tilde{v}$ and $\tilde{l}$, with results corresponding to $\lambda = 1.1$. These surfaces illustrate the influence of geometry on the mechanical response, demonstrating that multiple parameter combinations can yield similar auxetic behavior

parameters were incremented, each with 5 discrete values ($\tilde{l} = 1\ldots6, \tilde{v} = 1\ldots6$). This discrete elementary constant was denoted by k ($k = 0.1$). The parametrization is shown on line 6 and arc 2 from Fig. 10 in this order. The other objects were defined in a similar way. The two endpoints of line 6 are:

$$L_6^1 = (3 + (\tilde{v} - 1)k\ ;\ 3 - (\tilde{l} - 1)k)\,, \tag{6}$$

$$L_6^2 = (3 + (\tilde{v} - 1)k\ ;\ 5 + (\tilde{l} - 1)k)\,, \tag{7}$$

where the numerical values represent the original positions of the points, while the starting point of the line is the one located in the downstream horizontal direction. The parametrization of arc 2 is somewhat more complicated.

$$A_2^1 = (3 - (\tilde{l} - 1)k\ ;\ 1 - (\tilde{v} - 1)k)\,, \tag{8}$$

$$A_2^2 = (2 - (\tilde{l} - 1)k + (\tilde{v} - 1)k\ ;\ 0)\,. \tag{9}$$

In this case, the upper point represents the starting point and the lower point denotes the endpoint of the arc. Ultimately, we obtained 25 distinct models with varying geometries, examples of which are shown in Fig. 10.

The 25-25 features have been plotted on individual graphs, which can be seen in Fig. 11. The characters are similar in all cases, but the values vary greatly for different parameter combinations, demonstrating the significant influence of the shape and size of the perforations. It can also be observed that for a significant number of geometries, the Poisson's ratio does not take negative values at all or only over a very small range. This indicates that the structure in this case is not auxetic. Fig. 11c shows the stretch values at which we achieve a zero Poisson's ratio for different geometries.

As an illustration, Fig. 12 shows how the tensile force and Poisson's ratio depend on the $\tilde{v}$ and $\tilde{l}$ geometric parameters. To represent this dependence as a surface, the stretch value had to be fixed at a given level. In subfigure **a**, the stretch value is 1.8, while in subfigure (b), it is 1.1. It should be noted that different stretch values correspond to different surfaces. Analytical functions could be fitted to these surfaces, but simple interpolation can also be used to determine the required $\tilde{\nu}$ and $\tilde{l}$ values for achieving a given Poisson's ratio at a specified stretch. As the results indicate, multiple solutions exist, as slicing the surface with a plane results in a curve. Although the surfaces shown in the figure may appear planar, they are not, and their nonlinearity strongly depends on the chosen stretch value.

5 Discussion

The methodology presented in this study is not limited to the specific auxetic structures examined but also contributes to a broader understanding of modeling challenges in auxetic materials. While numerous studies exist on auxetic structures, no comprehensive work provides a complete framework for addressing the design and modeling aspects systematically. The proposed methodology offers a structured approach to facilitate the targeted design and practical implementation of auxetic structures from an engineering perspective.

The good overall agreement between the finite element models and experimental measurements confirms the reliability of the numerical model. Finite element simulations are a valuable predictive tool, but experimental validation remains essential. The primary reasons for any discrepancies between the numerical and experimental results are discussed in the following paragraph.

Several factors may contribute to the observed differences between the experimental measurements and finite element simulations. Geometric idealizations in the numerical models, such as variations in the laser-cut specimen dimensions and sheet thickness, introduce small discrepancies. The idealized boundary conditions in the simulations assume perfect fixation, whereas minor slippage or deformation may occur in the clamping region during physical testing. Additionally, the assumption of plane stress in simulations does not fully capture the 3D stress state that may develop, particularly near constrained areas. Material modeling is another key factor. While we employed the most accurate hyperelastic model available in Abaqus, no material model can perfectly replicate experimental stress-strain behavior, especially under complex, non-homogeneous loading. Furthermore, viscoelastic effects were not considered in simulations, though they are expected to have a minimal influence due to the quasi-static nature of the experiments. The homogeneous and isotropic material assumption may also introduce minor deviations, although tensile tests confirmed that the material's properties were largely uniform. Additional sources of discrepancy include motion tracking accuracy in video-based strain measurements, which was minimized using high-resolution 8K recordings and optimized camera positioning. In this study, pixel-based measurements were utilized to calculate dimensionless quantities such as displacement and strain, a methodology inspired by widely adopted techniques like Digital Image Correlation (DIC). High-resolution 8K video recordings ensured precise data acquisition, while careful camera placement minimized parallax errors. This approach allowed for accurate strain measurements within the studied scale and facilitated direct comparison with finite element simulations. The methodology's scalability across different specimen sizes is supported by its dimensionless framework, and the challenges typically associated with scaling, such as resolution limitations or parallax effects, were not encountered in our setup. The Instron load cell used in the experiments has a high precision ensuring minimal measurement-induced deviations. Moreover, wrinkling effects in auxetic structures altered the deformation patterns, particularly at higher stretch values, which were not captured in the plane-stress FEM simulations [31, 33, 49, 50]. Lastly, environmental factors such as temperature and humidity remained constant throughout the experiments, ensuring that thermal effects were not a significant contributor to the deviations. These factors, individually small, collectively contribute to the differences between experimental and numerical results. However, the trends in both approaches remain highly consistent, demonstrating the robustness and reliability of the presented methodology.

The determination of Poisson's ratio in auxetic structures is not standardized, and its value is highly dependent on the measurement domain selected for evaluation. In this study, we provided a detailed explanation of the measurement methodology and the formula used to calculate Poisson's ratio, referencing relevant literature. The results indicate that Poisson's ratio exhibits a significant variation as a function of axial stretch, which is a crucial consideration for the design of auxetic structures.

The wrinkling phenomenon was systematically identified in the experimental tests, and the critical stretch value at which wrinkling occurs was quantified. Wrinkling affects transverse deformations and should be carefully considered when applying auxetic structures in practical scenarios. In certain applications, wrinkling may even be advantageous, as it allows for programmable shape transformations, as demonstrated in various studies.

The selected mesh density was found to be sufficient, as convergence was confirmed through a comparison with finer meshes. The analysis showed that further mesh refinement was unnecessary, as increasing the number of elements by a factor of ten resulted in deviations of less than 1%.

The methodology proposed in this study can be extended to other auxetic geometries and material types, including those exhibiting viscoelastic or anisotropic behavior. A promising direction for future research would be numerical optimization, where the optimal auxetic geometry is determined based on a specific objective function.

6 Conclusions

The methodology presented in this study enables the design of planar auxetic structures tailored to meet specific user requirements, ensuring that a given Poisson's ratio is achieved at a predefined stretch value. By comparing experimental results with finite element simulations, we demonstrated that the developed numerical model is reliable for the analyzed structures.

For all four examined auxetic structures, the wrinkling phenomenon was observed, primarily attributed to the applied boundary conditions. We showed that wrinkling can be identified without the need for side-view imaging during the experiments. Instead, we determined the stretch values at which wrinkling occurs purely through the analysis of single-direction video recordings and their comparison with finite element simulations.

We introduced a parametric analysis that quantifies the influence of individual geometric parameters on the Poisson's ratio for a selected structure. The sixth-order Ogden hyperelastic model used in the numerical calculations proved to be suitable for accurately describing the mechanical behavior of the investigated silicone sheet material.

Additionally, we extended our planar model to three-dimensional cases and, through a case study, provided a detailed analysis of a 3D auxetic cube, highlighting its anisotropic characteristics.

7 Appendix – auxetic cube

The content of this Section provides insight into the application of the constructed method. The example under inevstgation is a cube, designed with STR2 variations. The geometry is different for all axes of the three dimensional space, resulting in an anisotropic body. This feature may allow implementation in specific engineering applications, for instance as actuators in the field of soft robotics. The dimensions of the perforations were selected based on the results

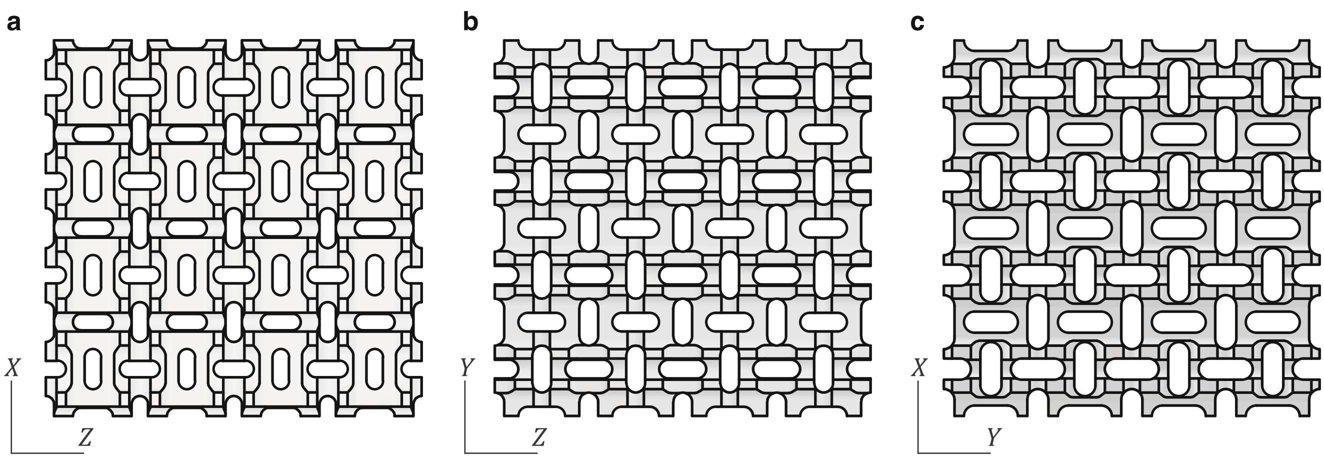

Fig. 13 Three different views of the 3D auxetic cube structure, illustrating its geometric configuration and structural design. The visualization highlights the repeating unit cells and the overall cellular nature of the cube

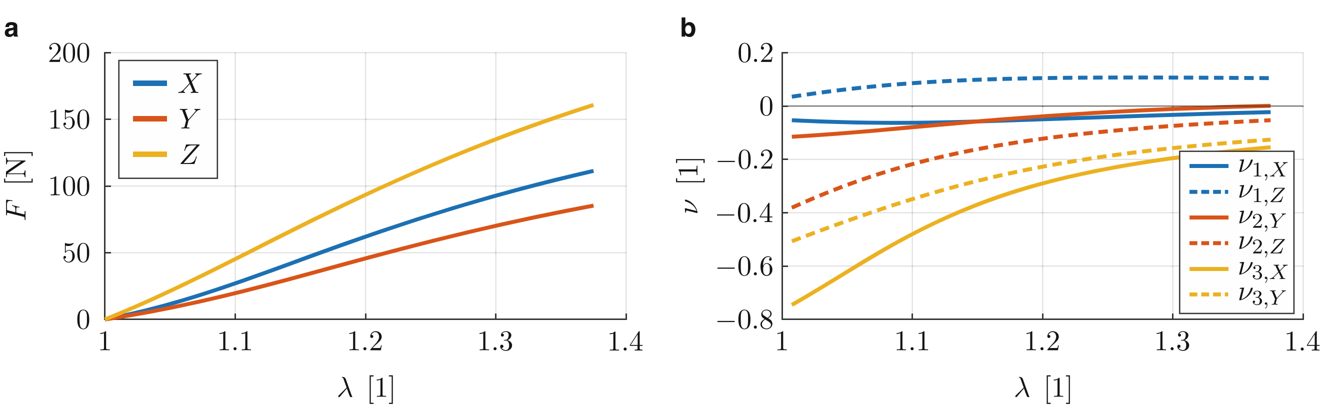

Fig. 14 Characteristics of the cube: **a** force-axial stretch functions, **b** Poisson's functions

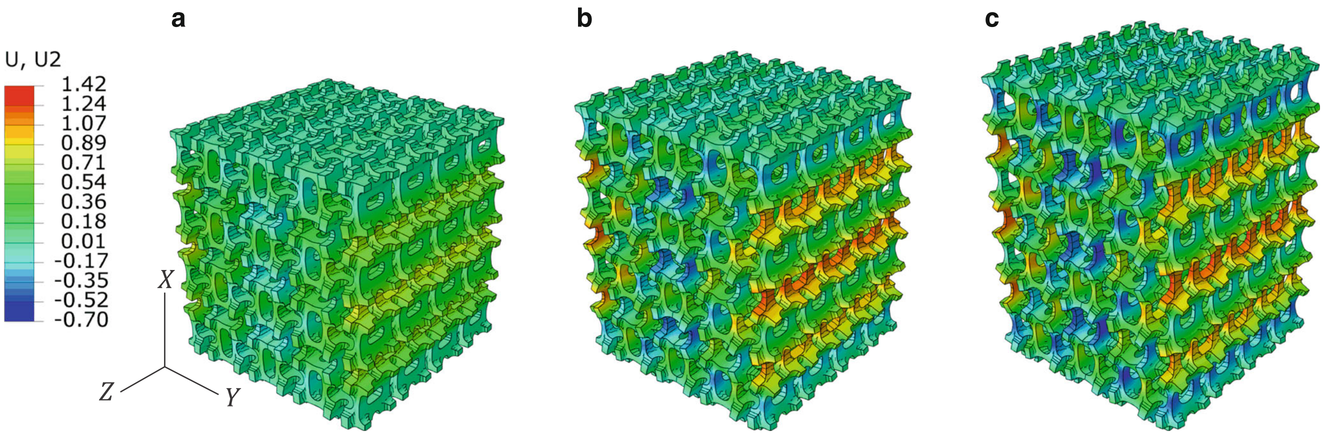

Fig. 15 Deformation of the cube for X directional loading: **a** $\lambda = 1.08$, **b** $\lambda = 1.23$, **c** $\lambda = 1.375$

of Sect. 4, with the geometries of Fig. 13. The objective was to select a structure that exhibited relatively strong auxetic behavior, one with near-zero Poisson's ratio, and one with a conventional behavior to the greatest extent possible. A body with a unit cell structure of $4\times4\times4$ was analyzed, resulting in a final cube dimension of $32\times32\times32$ mm.

The simulations are structured in a similar manner to those presented in Sect. 3. Three simulations were performed with different loading directions, and the properties were analyzed accordingly. To optimize the analyses, a $2\times2\times2$ instead of a $4\times4\times4$ structure was used, and the body was modeled by specifying the appropriate symmetries. The displacement is defined as 6 mm in each case, corresponding to a tensile load. This results in a total displacement of 12 mm due to the symmetry of the problem. In this case, tetrahedron elements must be employed. The C3D10H element is a 10-node quadratic tetrahedron with hybrid formulation that is employed to manage the incompressible material. The resulting force-axial stretch and Poisson's ratio functions are depicted in Fig. 14.

The symbols X, Y, and Z indicate the direction of the load, i.e., the stiffest structure is obtained for a load in the Z direction, followed by the X and Y directions. For a single model, two Poisson functions can be calculated depending on the loading direction, resulting in a total of six functions for three models. In Fig. 14, the same colours are associated with the same type of perforation, whereas the identical line styles correspond to the direction of loading. The curves for each plane in question are not identical, which indicates that these functions depend on the direction of the load. Consequently, we may conclude that the deformation of the cube is a coupled phenomenon from a mechanical point of view. Figure 15 presents a visual representation of the cube at three distinct stretch values during the loading process. The body is coloured according to the Y directional displacements.

Acknowledgements This research was supported by the Hungarian National Research, Development and Innovation Office (FK 142457). This research was supported by the János Bolyai Research Scholarship of the Hungarian Academy of Sciences.

Author contributions Both authors, Tamás Vargovics and Attila Kossa, contributed equally to all aspects of this study. This includes the conceptualization and design of the research, conducting experiments, developing and validating the numerical models, performing data analysis, and preparing the manuscript. Both authors have read and approved the final version of the manuscript.

Funding Open access funding provided by Budapest University of Technology and Economics.

Conflict of interest

The authors declare no potential conflict of interests.

None financial disclosure reported.

References

1. Balan MP, Mertens AJ, Bahubalendruni MVAR (2023) Auxetic mechanical metamaterials and their futuristic developments: A state-

of-art review. Mater Today Commun 34:105285. https://doi.org/10.1016/j.mtcomm.2022.105285
2. Zhang Z, Zhua H, Yuanb R, Wangb S, Fanc T, Rezguia Y, Zhangc D (2020) Auxetic interpenetrating composites: A new approach to non-porous materials with a negative or zero poisson's ratio. Compos Struct 243:112195. https://doi.org/10.1016/j.compstruct.2020.112195
3. Huang C, Chen L (2016) Negative poisson's ratio in modern functional materials. Adv Mater 28:8079–8096. https://doi.org/10.1002/adma.201601363
4. Abbaslou M, Hashemi R, Etemadi E (2023) Novel hybrid 3D-printed auxetic vascular stent based on re-entrant and meta-trichiral unit cells: Finite element simulation with experimental verifications. Mater Today Commun 35:105742. https://doi.org/10.1016/j.mtcomm.2023.105742
5. Vellaparambil R, Han WS, Di Giovanni P, Avril S (2024) Computational comparison of the mechanical behavior of aortic stent-grafts derived from auxetic unit cells. Cardiovasc Eng Tech 15:199–210. https://doi.org/10.1007/s13239-023-00706-x
6. Behinfar P, Nourani A (2024) Analytical and numerical solution and multi-objective optimization of tetra-star-chiral auxetic stents. Discov Appl Sci 6:39. https://doi.org/10.1007/s42452-024-05663-1
7. Jiang Y, Shi K, Zhou L, He M, Zhu C, Wang J, Li J, Li Y, Liu L, Sun D, Feng G, Yi Y, Zhang L (2020) 3d-printed auxetic-structured intervertebral disc implant for potential treatment of lumbar herniated disc. Bioact Mater 20:528–538. https://doi.org/10.1016/j.bioactmat.2022.06.002
8. Xu Y, Meng Z, Bol RJM, Šavija B (2024) Spring-like behavior of cementitious composite enabled by auxetic hyperelastic frame. Int J Mech Sci 109364:2024. https://doi.org/10.1016/j.ijmecsci.2024.109364
9. Zhang M, Xu J, Li D, Liu Y (2024) Node-reinforced design and selective remanufacturing of auxetic lattice structures. Adv Eng Mater 26:2302020. https://doi.org/10.1002/adem.202302020
10. Shepherd T, Winwood K, Venkatraman P, Alderson A, Allen T (2020) Validation of a finite element modeling process for auxetic structures under impact. Phys Status Solidi B 257:1900197. https://doi.org/10.1002/pssb.201900197
11. Ren X, Han D, Sun L, Zhang XG, Jiang W, Tao Z, Xie YM, Yang F, Lu GX (2023) Experimental and numerical investigations of aluminum foam-filled auxetic circular tubular metamaterials with elliptical cells. Constr Build Mater 374:130900. https://doi.org/10.1016/j.conbuildmat.2023.130900
12. Han D, Zhang Y, Zhang XY, Xie YM, Ren X (2023) Lightweight auxetic tubular metamaterials: Design and mechanical characteristics. Compos Struct 311:116849. https://doi.org/10.1016/j.compstruct.2023.116849
13. Wang Q, Yang Z, Lu Z, Li X (2020) Mechanical responses of 3d cross-chiral auxetic materials under uniaxial compression. Mater Des 186:108226. https://doi.org/10.1016/j.matdes.2019.108226
14. Faraci D, Driemeier L, Comi C (2021) Bending-dominated auxetic materials for wearable protective devices against impact. J Dyn Behav Mater 7:425–435. https://doi.org/10.1007/s40870-020-00284-2
15. Tomita S, Shimanuki K, Oyama S, Nishigaki H, Nakagawa T, Tsutsui M, Emura Y, Chino M, Tanaka H, Itou Y, Umemoto K (2023) Transition of deformation modes from bending to auxetic compression in origami-based metamaterials for head protection from impact. Sci Rep 13:12221. https://doi.org/10.1038/s41598-023-39200-8
16. Chang Y, Wang H, Dong Q (2022) Machine learning-based inverse design of auxetic metamaterial with zero poisson's ratio. Mater Today Commun 30:103186. https://doi.org/10.1016/j.mtcomm.2022.103186
17. Ebert M, Adhikari R, Hasan MK, Lupo K, Akleman E, Pharr M, Krishnamurthy VR (2024) Abc-auxetics: An implicit design approach for negative poisson‘s ratio materials. Adv Eng Mater 26:1438–1656. https://doi.org/10.1002/adem.202301359
18. Grossi B, Palza H, Zagal JC, Falcón C, During G (2021) Metarpillar: Soft robotic locomotion based on buckling-driven elastomeric metamaterials. Mater Des 212:110285. https://doi.org/10.1016/j.matdes.2021.110285
19. Pan Q, Chen S, Chen F, Zhu X (2020) Programmable soft bending actuators with auxetic metamaterials. Sci China Technol Sci 63:2518–2526. https://doi.org/10.1007/s11431-020-1741-2
20. Lee Y, Misra S, Chen W, Koditschek DE, Sung C, Yang S (2022) Tendon-driven auxetic tubular springs for resilient hopping robots. Adv Intell Syst 4:2640–4567. https://doi.org/10.1002/aisy.202100152
21. Grima-Cornish JN, Grima JN, Attard D (2021) Mathematical modeling of auxetic systems: bridging the gap between analytical models and observation. Int J Mech Mater Eng 16:4. https://doi.org/10.1186/s40712-020-00125-z
22. Srivastava C, Bhola L, Mahesh V, Guruprasad PJ, Petrinic N, Scarpa F, Harursampath D, Ponnusami SA (2023) Exploiting nonlinearities through geometric engineering to enhance the auxetic behaviour in re-entrant honeycomb metamaterials. Sci Rep 23:20915. https://doi.org/10.1038/s41598-023-47525-7
23. Rafsanjani A, Pasinib D (2016) Bistable auxetic mechanical metamaterials inspired by ancient geometric motifs. Extreme Mech Lett 9:291–296. https://doi.org/10.1016/j.eml.2016.09.001
24. McHale G, Alderson A, Armstrong S, Mandhani S, Meyari M, Wells GG, Carter E, Ledesma-Aguilar R, Semprebon C, Evans K (2024) Transforming auxetic metamaterials into superhydrophobic surfaces. Small Struct 5:2300458. https://doi.org/10.1002/sstr.202300458
25. Park YJ, Ahn H, Rodrigue H (2024) Shape-memory alloy-based auxetic smart metamaterials: Enabling inherently bidirectional actuation. Adv Intell Syst. https://doi.org/10.1002/aisy.202400040
26. Dara A, Bahubalendruni MVAR, Mertens AJ, Balamurali G (2022) Numerical and experimental investigations of novel nature inspired open lattice cellular structures for enhanced stiffness and specific energy absorption. Mater Today Commun 31:103286. https://doi.org/10.1016/j.mtcomm.2022.103286
27. Dara A, Bahubalendruni MVAR, Mertens AJ, Balamurali G (2022) A novel nature inspired 3D open lattice structure for specific energy absorption. Proc Inst Mech Eng Part E: J Process Mech Eng 236(6):2434–2440. https://doi.org/10.1177/09544089221092894
28. Dara A, Bahubalendruni MVAR (2023) Design and characterization of 2.5D nature-inspired infill structures under out-plane quasi-static loading condition. Adv Mater Sci Eng 2023(1):8918937. https://doi.org/10.1155/2023/8918937
29. Hamzehei R, Kadkhodapour J, Anaraki AP, Rezaei S, Dariushi S, Rezadoust AM (2018) Octagonal auxetic metamaterials with hyperelastic properties for large compressive deformation. Int J Mech Sci 145:96–105. https://doi.org/10.1016/j.ijmecsci.2018.06.040
30. Lotfi J, Khalili SMR, Damanpack AR (2024) Micro-macro analysis of hyperelastic auxetic lattice structures under finite-strain regime. Int J Mech Sci 274:109246. https://doi.org/10.1016/j.ijmecsci.2024.109246
31. Rezaei S, Kadkhodapour J, Hamzehei R, Taherkhani B, Pourkamali Anaraki A, Dariushi S (2021) Design and modeling of the 2d auxetic metamaterials with hyperelastic properties using topology optimization approach. Photonics Nanostructures - Fundam Appl 43:100868. https://doi.org/10.1016/j.photonics.2020.100868
32. Wilt JK, Yang C, Gu GX (2020) Accelerating auxetic metamaterial design with deep learning. Adv Eng Mater 22:1901266. https://doi.org/10.1002/adem.201901266
33. Uddin KZ, Pagliocca N, Anni IA, Youssef G, Koohbor B (2023) Multiscale strain field characterization in flexible planar auxetic

metamaterials with rotating squares. Adv Eng Mater 25:2201248. https://doi.org/10.1002/adem.202201248
34. Angeloni C, Liverani E, Ascari A, Fortunato A (2024) Characterization and process optimization of remote laser cutting of current collectors for battery electrode production. J Mater Process Technol 324:118266. https://doi.org/10.1016/j.jmatprotec.2023.118266
35. Laser cutting machine. Unisonic Kft., Dunaharaszti, Hungary. https://www.alfalaser.hu/
36. Floch K, Kossa A (2023) Motion tracker beta: A gui based open-source motion tracking application. SoftwareX 23(23):101424. https://doi.org/10.1016/j.softx.2023.101424
37. Dilek AY, Buket OB (2022) Measurement of poisson's ratio of the auxetic structure. Measurement 204:112040. https://doi.org/10.1016/j.measurement.2022.112040
38. Beatty MF (1987) Topics in finite elasticity: Hyperelasticity of rubber, elastomers, and biological tissues with examples. Appl Mech Rev 40:1699–1734. https://doi.org/10.1115/1.3149545
39. Lührs L, Soyarslan C, Markmann J, Bargmann S, Weissmüller J (2016) Elastic and plastic poisson's ratios of nanoporous gold. Scr Mater 110:65–69. https://doi.org/10.1016/j.scriptamat.2015.08.002
40. Ho DT, Park S-D, Kwon S-Y, Han T-S, Kim SY (2016) Negative poisson‘s ratio in cubic materials along principal directions. Phys Status Solidi (b) 253(7):1288–1294. https://doi.org/10.1002/pssb.201600017
41. Scott NH (2007) The incremental bulk modulus, young‘s modulus and poisson‘s ratio in nonlinear isotropic elasticity: Physically reasonable response. Math Mech Solids 12(5):526–542. https://doi.org/10.1177/1081286506064719
42. Picu RC, Deogekar S, Islam MR (2018) Poisson‘s contraction and fiber kinematics in tissue: Insight from collagen network simulations. J Biomech Eng 140(2):210021–2100212. https://doi.org/10.1115/1.4038428
43. Gatt R, Wood MV, Gatt A, Zarb F, Formosa C, Azzopardi KM, Casha A, Agius TP, Schembri-Wismayer P, Attard L, Chockalingam N, Grima JN (2015) Negative poisson's ratios in tendons: An unexpected mechanical response. Acta Biomater 24:201–208. https://doi.org/10.1016/j.actbio.2015.06.018
44. Shivers JL, Arzash S, MacKintosh FC (2020) Nonlinear poisson effect governed by a mechanical critical transition. Phys Rev Lett 124:38002. https://doi.org/10.1103/PhysRevLett.124.038002
45. Ouardi A, Boukamel A, Damil N (2023) A model for hyperelastic rubber-like materials based on micro-mechanical elements. Eur J Mech 101:105036. https://doi.org/10.1016/j.euromechsol.2023.105036
46. Treloar LRG (1944) Stress-strain data for vulcanized rubber under various types of deformation. Rubber Chem Technol 17(4):813–825. https://doi.org/10.5254/1.3546701
47. Dara A, Mertens AJ, Bahubalendruni MVAR (2023) Characterization of penetrate and interpenetrate tessellated cellular lattice structures for energy absorption. Proc Inst Mech Eng Part L: J Materials: Des Appl 237(4):906–913. https://doi.org/10.1177/14644207221129709
48. Dara A, Bahubalendruni MVAR, Mhaskar A, Choudhary V, Balamurali G, Turaka S (2023) Experimental and numerical investigation on 2.5-dimensional nature-inspired infill structures under outplane quasi-static loading. Proc Inst Mech Eng Part E: J Process Mech Eng 0(0):1–11. https://doi.org/10.1177/09544089231197853
49. Gupta S, Gupta V, Chanda A (2022) Biomechanical modeling of novel high expansion auxetic skin grafts. Numer Methods Biomed Eng 38:e3586. https://doi.org/10.1002/cnm.3586
50. Rita de Carvalho V (2015) Wrinkling of thin sheets under tension. Instituto Superior Técnico, Lisboa, Portugal (Master‘s thesis)

Supporting information Additional supporting information may be found in the online version of the article at the publishers website.